Cantilever Beam Design for Projectile Internal Moving Mass Systems

Jonathan Rogers
Graduate Research Assistant

Mark Costello
Sikorsky Associate Professor
Mem. ASME

School of Aerospace Engineering,
Georgia Institute of Technology,
Atlanta, GA 30318

Internal masses that undergo controlled translation within a projectile have been shown to be effective control mechanisms for smart weapons. However, internal mass oscillation must occur at the projectile roll frequency to generate sufficient control force. This can lead to high power requirements and place a heavy burden on designers attempting to allocate volume within the projectile for internal mass actuators and power supplies. The work reported here outlines a conceptual design for an internal translating mass system using a cantilever beam and electromagnetic actuators. The cantilever beam acts as the moving mass, vibrating at the projectile roll frequency to generate control force. First, a dynamic model is developed to describe the system. Then the natural frequency, damping ratio, and length of the beam are varied to study their affects on force required and total battery size. Trade studies also examine the effect on force required and total battery size of a roll-rate feedback system that actively changes beam elastic properties. Results show that, with proper sizing and specifications, the cantilever beam control mechanism requires relatively small batteries and low actuator control forces with minimum actuator complexity and space requirements. [DOI: 10.1115/1.3155017]

1 Introduction

The past several decades have seen growing interest in the development of smart munitions resulting from attempts to increase accuracy and to decrease collateral damage. Smart projectiles differ from other guided weapons, such as guided missiles, in that their electronics and control mechanisms must be able to withstand extreme acceleration loads associated with launch and high spin rates. Control components must be relatively inexpensive, since projectiles are typically fired in large quantities. Several different types of control mechanisms have been designed to meet these requirements, namely, aerodynamic mechanisms, thrust mechanisms, and inertial load mechanisms. Common examples of aerodynamic mechanisms are canards, gimbaled nose configurations, and deflection of ram air through side ports. Examples of thrust mechanisms include cold gas jets and explosive thrusters. Examples of inertial load mechanisms are rotation of an unbalanced internal part and, of specific interest here, movement of an internal translating mass (ITM). Oscillation of an internal mass at the projectile roll frequency has been shown to produce useful control authority. A design that minimizes moving parts and substantially reduces power required is critical in order to physically implement an ITM control mechanism on board a smart munition.

Previous investigation of projectiles equipped with loose or moving internal parts has revealed that these configurations can result in flight instabilities. Soper [1] considered the stability of a projectile with a cylindrical mass fitted loosely within a cavity. Murphy [2], using a similar configuration, derived a quasilinear solution for the motion of a projectile equipped with a moving internal part. A detailed set of experiments was later conducted by D'Amico [3] to model the motion of internal masses within spinning projectiles using a freely-gimbaled gyroscope. Hodapp [4] further considered the affect of a small offset between the projectile body mass and the ITM mass center. Hodapp's analysis of the dynamic equations for this system showed that, for small mass center offsets, slight movement could actually reduce the instability caused by the loose internal part. The use of controlled movement of an ITM as a maneuver control mechanism was considered by Petsopoulous et al. [5] for use on re-entry vehicles, while Robinett et al. [6] considered ITM control for ballistic rockets. More recently, Menon et al. [7] examined ITM control for use on endo- and exoatmospheric interceptors using three orthogonal ITMs. Frost and Costello [8,9] studied the ability of an internal rotating mass unbalance to actively control both fin and spin-stabilized projectiles. Most recently, Rogers and Costello [10] investigated control authority of a projectile equipped with a single internal translating mass. It was determined that significant control authority could be created by oscillating the ITM at the projectile roll frequency.

This paper outlines a notional design of an ITM actuator that generates sufficient control authority using relatively low power. Control moment is generated due to an axial drag offset from the system mass center caused by the lateral motion of the ITM. This paper begins with a description of the cantilever beam system that serves as the translating mass, and derives the seven-degree of freedom flight dynamic model used for trajectory predictions. A description of the control law and ITM electromagnetic actuators are also provided. The dynamic model is subsequently employed to demonstrate that the cantilever beam configuration provides sufficient control authority at reasonable power levels. Trade studies examine the effect of cantilever beam length on force required and battery size. The optimum natural frequency and damping ratio of the beam is determined in order to minimize actuator control effort. Finally, roll-rate feedback control is implemented to actively alter beam characteristics as the projectile roll rate changes during flight, further decreasing the control effort required. A final example case demonstrates that sufficient control authority can be generated with relatively small battery sizes using the optimum spring and damper coefficients and the roll-rate feedback system.

2 Cantilever Beam Projectile Dynamic Model

The cantilever beam is a fixed-free elastic beam, with one end attached to the projectile at point L and the free end floating within the cavity, constrained to vibrate in the $\vec{I}_S - \vec{J}_S$ plane. The beam's first vibrational mode is the only mode considered signifi-

Contributed by the Dynamic Systems, Measurement, and Control Division of ASME for publication in the JOURNAL OF DYNAMIC SYSTEMS, MEASUREMENT, AND CONTROL. Manuscript received October 29, 2008; final manuscript received May 4, 2009; published online August 18, 2009. Assoc. Editor: Ahmet S. Yigit.

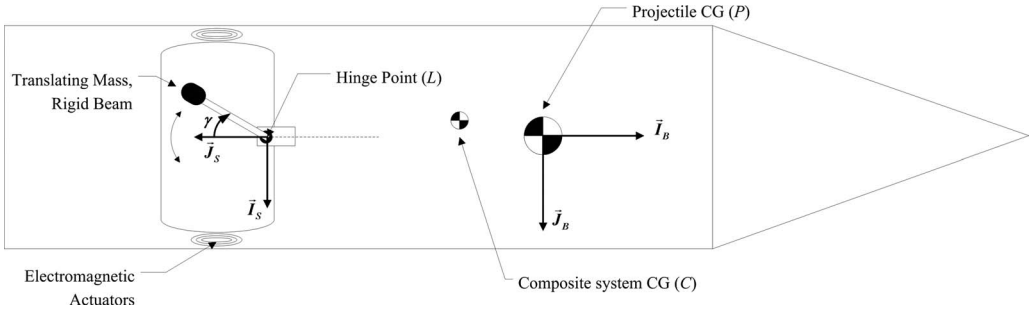

Fig. 1 The ITM-beam projectile

cant to dynamic interaction with the projectile. For this reason, the cantilever beam can be accurately modeled as a rigid massless beam with a spherical mass (considered to be a permanent magnet) attached to the end. A torsional spring and damper are attached to the hinge point to simulate the elastic properties of the cantilever beam. This dynamically equivalent system is referred to as the ITM-beam. A sketch of this configuration is shown in Fig. 1. Note that γ is defined as the angle between the ITM-beam and the centerline of the projectile. A permanent magnet is attached to the end of the beam and can swing freely about the hinge. Force is exerted on the magnet by electromagnets on both sides of the cavity to move the beam to a desired angle.

Five reference frames are used in the development of the equations of motion for this system, namely, the inertial, projectile, translating mass, nonrolling, and projectile-fixed S reference frames. The projectile frame is obtained using the standard aerospace Euler angle sequence of rotations, and is related to the inertial frame by

$$\begin{Bmatrix} \vec{I}_B \\ \vec{J}_B \\ \vec{K}_B \end{Bmatrix} = \begin{bmatrix} c_\theta c_\psi & c_\theta s_\psi & -s_\theta \\ s_\phi s_\theta c_\psi - c_\phi s_\psi & s_\phi s_\theta s_\psi + c_\phi c_\psi & s_\phi c_\theta \\ c_\phi s_\theta c_\psi + s_\phi s_\psi & c_\phi s_\theta s_\psi - s_\phi c_\psi & c_\phi c_\theta \end{bmatrix} \begin{Bmatrix} \vec{I}_I \\ \vec{J}_I \\ \vec{K}_I \end{Bmatrix} \tag{1}$$

The N frame is the standard nonrolling reference frame often used in projectile flight dynamics, and is defined by a rotation of $-\phi$ along the $\vec{I}_B$ axis. The S frame is also fixed to the projectile, with its origin at the hinge point. It is defined such that the ITM-beam oscillates about the $\vec{K}_S$ axis, and $\vec{J}_S$ points to the rear of the cavity exactly equidistant from both electromagnetic actuators. Therefore, the S frame can be related to the B frame by two constant Euler angles ψ_S and θ_S such that

$$\begin{Bmatrix} \vec{I}_S \\ \vec{J}_S \\ \vec{K}_S \end{Bmatrix} = \begin{bmatrix} c_{\theta_S} c_{\psi_S} & c_{\theta_S} s_{\psi_S} & -s_{\theta_S} \\ -s_{\psi_S} & c_{\psi_S} & 0 \\ s_{\theta_S} c_{\psi_S} & s_{\theta_S} s_{\psi_S} & c_{\theta_S} \end{bmatrix} \begin{Bmatrix} \vec{I}_B \\ \vec{J}_B \\ \vec{K}_B \end{Bmatrix} \tag{2}$$

Throughout the rest of this article, fixed angles of $\psi_S = 90$ deg and $\theta_S = 0$ are used, and thus the S frame can be obtained by a single 90 deg rotation about the $\vec{K}_B$ axis, resulting in the orientation shown in Fig. 1. The T frame is fixed to the ITM-beam and is related to the S frame by the relationship

$$\begin{Bmatrix} \vec{I}_T \\ \vec{J}_T \\ \vec{K}_T \end{Bmatrix} = \begin{bmatrix} c_\gamma & s_\gamma & 0 \\ -s_\gamma & c_\gamma & 0 \\ 0 & 0 & 1 \end{bmatrix} \begin{Bmatrix} \vec{I}_S \\ \vec{J}_S \\ \vec{K}_S \end{Bmatrix} \tag{3}$$

Note that the T frame is aligned with the S frame when $\gamma = 0$. All equations in this paper use the following shorthand notation for trigonometric sine, cosine, and tangent functions: $s_\alpha = \sin\alpha$, $c_\alpha = \cos\alpha$, and $t_\alpha = \tan\alpha$.

Throughout the development of the equations of motion, two operators will be used to denote components of a vector in a specific frame and the skew symmetric cross-product operator, respectively. The vector component operator outputs a column vector comprised of the components of an input vector in a given frame. For example, if the position vector from α to β is expressed in reference frame A as $\vec{r}_{\alpha\to\beta} = \Delta x_{\alpha\beta}\vec{I}_A + \Delta y_{\alpha\beta}\vec{J}_A + \Delta z_{\alpha\beta}\vec{K}_A$ then the vector component operator acting on this vector yields

$$\mathbb{C}_A(\vec{r}_{\alpha\to\beta}) = \begin{Bmatrix} \Delta x_{\alpha\beta} \\ \Delta y_{\alpha\beta} \\ \Delta z_{\alpha\beta} \end{Bmatrix} \tag{4}$$

Notice that the reference frame is denoted by the subscript on the operator. The cross-product operator outputs a skew symmetric matrix using the components of an input vector in the reference frame denoted in the subscript. For example, if the position vector from α to β is expressed in reference frame A as $\vec{r}_{\alpha\to\beta} = \Delta x_{\alpha\beta}\vec{I}_A + \Delta y_{\alpha\beta}\vec{J}_A + \Delta z_{\alpha\beta}\vec{K}_A$ then the cross-product operator acting on $\vec{r}_{\alpha\to\beta}$ expressed in reference frame A is

$$\mathbb{S}_A(\vec{r}_{\alpha\to\beta}) = \begin{bmatrix} 0 & -\Delta z_{\alpha\beta} & \Delta y_{\alpha\beta} \\ \Delta z_{\alpha\beta} & 0 & -\Delta x_{\alpha\beta} \\ -\Delta y_{\alpha\beta} & \Delta x_{\alpha\beta} & 0 \end{bmatrix} \tag{5}$$

2.1 Kinematics. The velocity of the composite body mass center can be described in the inertial frame or the projectile reference frame

$$\vec{v}_{C/I} = \dot{x}\vec{I}_I + \dot{y}\vec{J}_I + \dot{z}\vec{K}_I = u\vec{I}_B + v\vec{J}_B + w\vec{K}_B \tag{6}$$

The translational kinematic differential equations relate these two representations of the mass center velocity components

$$\begin{Bmatrix} \dot{x} \\ \dot{y} \\ \dot{z} \end{Bmatrix} = \begin{bmatrix} c_\theta c_\psi & s_\phi s_\theta c_\psi - c_\phi s_\psi & c_\phi s_\theta c_\psi + s_\phi s_\psi \\ c_\theta s_\psi & s_\phi s_\theta s_\psi + c_\phi c_\psi & c_\phi s_\theta s_\psi - s_\phi c_\psi \\ -s_\theta & s_\phi c_\theta & c_\phi c_\theta \end{bmatrix} \begin{Bmatrix} u \\ v \\ w \end{Bmatrix} \tag{7}$$

The angular velocity of the projectile with respect to the inertial reference frame can be written in terms of appropriate Euler angle time derivatives or in terms of projectile frame angular velocity components

$$\vec{\omega}_{B/I} = \dot{\phi}\vec{I}_B + \dot{\theta}\vec{J}_N + \dot{\psi}\vec{K}_I = p\vec{I}_B + q\vec{J}_B + r\vec{K}_B \tag{8}$$

The kinematic relationship between time derivatives of the Euler angles and projectile reference frame angular velocity components represents the rotational kinematic differential equations

$$\begin{Bmatrix} \dot{\phi} \\ \dot{\theta} \\ \dot{\psi} \end{Bmatrix} = \begin{bmatrix} 1 & s_\phi t_\theta & c_\phi t_\theta \\ 0 & c_\phi & -s_\phi \\ 0 & s_\phi / c_\theta & c_\phi / c_\theta \end{bmatrix} \begin{Bmatrix} p \\ q \\ r \end{Bmatrix} \tag{9}$$

The final kinematic differential equation is the trivial relationship

$$\dot{\gamma} = \omega_{\text{beam}} \tag{10}$$

2.2 Dynamics. The translational dynamic equations for the ITM-beam projectile are derived through force balancing. Force balance equations for the projectile and ITM-beam are given, respectively, as

$$\boldsymbol{m_P}\vec{\boldsymbol{a}}_{\boldsymbol{P/I}} = \vec{\boldsymbol{W}}_{\boldsymbol{P}} + \vec{\boldsymbol{F}}_{\boldsymbol{P}} - \vec{\boldsymbol{F}}_{\boldsymbol{C}} - \vec{\boldsymbol{F}}_{\boldsymbol{I}} \tag{11}$$

$$\boldsymbol{m_T}\vec{\boldsymbol{a}}_{\boldsymbol{X/I}} = \vec{\boldsymbol{W}}_{\boldsymbol{T}} + \vec{\boldsymbol{F}}_{\boldsymbol{C}} + \vec{\boldsymbol{F}}_{\boldsymbol{I}} \tag{12}$$

where $\boldsymbol{m_P}$ and $\boldsymbol{m_T}$ are the masses of the projectile and ITM-beam, respectively; $\vec{\boldsymbol{a}}_{\boldsymbol{P/I}}$ and $\vec{\boldsymbol{a}}_{\boldsymbol{X/I}}$ are, respectively, the accelerations of points P and X with respect to the inertial frame; and $\vec{\boldsymbol{W}}_{\boldsymbol{P}}$, $\vec{\boldsymbol{W}}_{\boldsymbol{T}}$, $\vec{\boldsymbol{F}}_{\boldsymbol{P}}$, $\vec{\boldsymbol{F}}_{\boldsymbol{I}}$, and $\vec{\boldsymbol{F}}_{\boldsymbol{C}}$ are the weights of the projectile and ITM-beam, the total aerodynamic force exerted on the projectile, the input force exerted on the ITM-beam by the actuators, and the hinge constraint force, respectively. The definition of the system center of mass leads to

$$\boldsymbol{m}\vec{\boldsymbol{a}}_{\boldsymbol{C/I}} = \boldsymbol{m_P}\vec{\boldsymbol{a}}_{\boldsymbol{P/I}} + \boldsymbol{m_T}\vec{\boldsymbol{a}}_{\boldsymbol{X/I}} \tag{13}$$

Therefore, adding Eqs. (11) and (12) and noting the relationship in Eq. (13), the translational dynamic equation for the system is formed

$$\boldsymbol{m}\vec{\boldsymbol{a}}_{\boldsymbol{C/I}} = \vec{\boldsymbol{W}}_{\boldsymbol{P}} + \vec{\boldsymbol{W}}_{\boldsymbol{T}} + \vec{\boldsymbol{F}}_{\boldsymbol{P}} \tag{14}$$

The aerodynamic forces given by $\vec{\boldsymbol{F}}_{\boldsymbol{P}}$ in Eq. (14) are obtained using the standard aerodynamic expansion employed for projectile flight dynamic simulation. Both steady aerodynamic forces and Magnus forces are included, as well as steady and unsteady aerodynamic moments. The aerodynamic coefficients and aerodynamic center distances used to generate these forces and moments are all a function of the local Mach number at the center of mass of the projectile. Computationally, these Mach number dependent parameters are obtained by a table look-up scheme using linear interpolation. A full description of the weight force and body aerodynamic forces and moments are provided in Ref. [10]. Writing Eq. (14) in the projectile reference frame yields

$$\begin{Bmatrix} \dot{u} \\ \dot{v} \\ \dot{w} \end{Bmatrix} = \begin{Bmatrix} \dfrac{X_B}{m} \\ \dfrac{Y_B}{m} \\ \dfrac{Z_B}{m} \end{Bmatrix} - \begin{bmatrix} 0 & -r & q \\ r & 0 & -p \\ -q & p & 0 \end{bmatrix} \begin{Bmatrix} u \\ v \\ w \end{Bmatrix} \tag{15}$$

Note that $\boldsymbol{X_B}$, $\boldsymbol{Y_B}$, and $\boldsymbol{Z_B}$ are projectile reference frame components of the sum of the three forces given in Eq. (14).

The rotational dynamic equations are obtained by first equating the I frame time rate of change of the system angular momentum about the system mass center to the total applied external moments on the system about the system mass center in the $\vec{\boldsymbol{I}}_{\boldsymbol{S}}$ and $\vec{\boldsymbol{J}}_{\boldsymbol{S}}$ directions, given by Eqs. (16) and (17). Then, the same moment equation is used for each body separately, this time written in the $\vec{\boldsymbol{K}}_{\boldsymbol{S}}$ direction. These four equations are given by

$$\vec{I}_S \bullet \left(\frac{{}^P d\vec{H}^P_{B/I}}{dt} + \frac{{}^I d\vec{H}^X_{T/I}}{dt} + \vec{r}_{L\to P} \times m_P \vec{a}_{P/I} + \vec{r}_{L\to X} \times m_T \vec{a}_{X/I} \right) = \vec{I}_S \bullet \sum M^L_{\text{system}} \tag{16}$$

$$\vec{J}_S \bullet \left(\frac{{}^I d\vec{H}^P_{B/I}}{dt} + \frac{{}^I d\vec{H}^X_{T/I}}{dt} + \vec{r}_{L\to P} \times m_P \vec{a}_{P/I} + \vec{r}_{L\to X} \times m_T \vec{a}_{X/I} \right) = \vec{J}_S \bullet \sum M^L_{\text{system}} \tag{17}$$

$$\vec{K}_S \bullet \left(\frac{{}^I d\vec{H}^X_{T/I}}{dt} + \vec{r}_{L\to X} \times m_T \vec{a}_{X/I} \right) = -f_{\text{input}} BLc_\gamma + \vec{K}_S \bullet \mathbb{S}(\vec{r}_{L\to X}) \mathbb{C}_S(\vec{W}_T) + k_T \gamma + k_D \dot{\gamma} \tag{18}$$

$$\vec{K}_S \bullet \left(\frac{{}^I d\vec{H}^P_{B/I}}{dt} + \vec{r}_{L\to P} \times m_P \vec{a}_{P/I} \right) = f_{\text{input}} BLc_\gamma + \vec{K}_S \bullet \mathbb{S}(\vec{r}_{L\to P}) \mathbb{C}_S(\vec{W}_P) - k_T \gamma - k_D \dot{\gamma} + \vec{K}_S \bullet \mathbb{C}_S(\Sigma M^L_P) \tag{19}$$

whereas before $c_\gamma = \cos(\gamma)$. Note that Eq. (18) equates the time rate of change of the angular momentum of the ITM-beam to the total moment applied to the ITM-beam. Equation (19) equates the time rate of change of the angular momentum of the projectile to the total moment applied to the projectile.

Several intermediate expressions will be useful in deriving the rotational dynamic equations in the body-fixed S frame. First, note that the well-known two points fixed on a rigid body formula yields the relationship

$$\vec{\boldsymbol{a}}_{\boldsymbol{X/I}} = \vec{\boldsymbol{a}}_{\boldsymbol{C/I}} + \frac{\boldsymbol{m_P}}{\boldsymbol{m}} [\vec{\alpha}_{B/I} \times \vec{\boldsymbol{r}}_{P\to L} + \vec{\alpha}_{T/I} \times \vec{\boldsymbol{r}}_{L\to X} + \vec{\omega}_{B/I} \times \vec{\omega}_{B/I} \times \vec{\boldsymbol{r}}_{P\to L} + \vec{\omega}_{T/I} \times \vec{\omega}_{T/I} \times \vec{\boldsymbol{r}}_{L\to X}] \tag{20}$$

Equation (20) is used to expand $\vec{\boldsymbol{a}}_{\boldsymbol{X/I}}$ in terms of known quantities and state derivatives. Also, using the definition of the system center of mass, it can be shown through algebraic manipulation that

$$\vec{\boldsymbol{r}}_{\boldsymbol{L\to P}} \times \boldsymbol{m_P}\vec{\boldsymbol{a}}_{\boldsymbol{P/I}} + \vec{\boldsymbol{r}}_{\boldsymbol{L\to X}} \times \boldsymbol{m_T}\vec{\boldsymbol{a}}_{\boldsymbol{X/I}} = \vec{\boldsymbol{r}}_{\boldsymbol{L\to P}} \times \boldsymbol{m}\vec{\boldsymbol{a}}_{\boldsymbol{C/I}} + \vec{\boldsymbol{r}}_{\boldsymbol{P\to X}} \times \boldsymbol{m_T}\vec{\boldsymbol{a}}_{\boldsymbol{X/I}} \tag{21}$$

Equation (21) is also used to expand the cross-product terms on the left-hand side of Eqs. (16) and (17) in terms of known quantities and state derivatives.

Equations (16)–(19) can be expanded using the expressions in Eqs. (20) and (21) and rearranged to form a 4×4 system of equations given by

$$\begin{bmatrix} A_{11} & A_{12} & A_{13} & A_{14} \\ A_{21} & A_{22} & A_{23} & A_{24} \\ A_{31} & A_{32} & A_{33} & A_{34} \\ A_{41} & A_{42} & A_{43} & A_{44} \end{bmatrix} \begin{bmatrix} \dot{\tilde{p}} \\ \dot{\tilde{q}} \\ \dot{\tilde{r}} \\ \ddot{\gamma} \end{bmatrix} = \begin{bmatrix} B_1 \\ B_2 \\ B_3 \\ B_4 \end{bmatrix} \tag{22}$$

In Eq. (22), rows 1–4 correspond to Eqs. (16)–(19), respectively. The full expressions for the values of the A matrix and the B vector are lengthy and are provided in Appendix A. The set of equations given by Eqs. (7), (9), (10), (15), and (22) constitute the equations of motion for the ITM-beam projectile. Given a known set of initial conditions, these 14 scalar equations are numerically integrated forward in time using a fourth-order Runge–Kutta algorithm to obtain a single trajectory.

2.3 Description of Controller. In order to create trajectory alterations, the ITM-beam must be moved in a prescribed manner. The control law is formulated based on a feedback linearization technique [11], which assumes full state feedback. Equation (23) is used to compute the control force, $\boldsymbol{f}_{\text{input}}$, required to deflect the ITM-beam to the desired angle.

$$\boldsymbol{f}_{\text{input}} = \frac{-1}{\boldsymbol{BLc}_\gamma} [\boldsymbol{B_{FLC}} - \boldsymbol{A}_{11}\dot{\tilde{\boldsymbol{p}}} - \boldsymbol{A}_{12}\dot{\tilde{\boldsymbol{q}}} - \boldsymbol{A}_{13}\dot{\tilde{\boldsymbol{r}}} - \boldsymbol{A}_{14}\ddot{\gamma}] - \boldsymbol{K}_0 \ddot{\gamma}_{\text{command}} - \boldsymbol{K}_1(\dot{\gamma}_{\text{command}} - \dot{\gamma}) - \boldsymbol{K}_2(\gamma_{\text{command}} - \gamma) \tag{23}$$

Note that $\boldsymbol{B_{FLC}}$ is defined in Appendix A and is derived from Eq. (18). Likewise, $\boldsymbol{A}_{11}$, $\boldsymbol{A}_{12}$, $\boldsymbol{A}_{13}$, and $\boldsymbol{A}_{14}$ are from Eq. (18) and provided in Appendix A. Note that Eq. (18) is used to compute the feedback linearization control, rather than Eq. (19), since Eq. (19) would require feedback of aerodynamic loads. This is a compli-

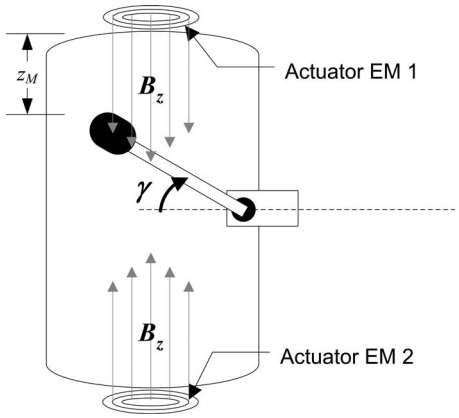

Fig. 2 Zoom view of the ITM-beam system

cated task and can be avoided through the use of Eq. (18) instead.

The commanded deflection angle γ_{command} is generated by synchronizing ITM-beam movement with the projectile roll angle. This is done by setting

$$\gamma_{\text{command}} = \sin^{-1}\left(-\frac{A}{BL}\cos(\phi + \phi_T)\right) \tag{24}$$

where A is the magnitude of oscillation of point X from the cavity center, and ϕ_T is a trim angle used to define the plane of control. Derivatives of Eq. (24) are computed analytically and used in Eq. (23). Note that the feedback linearization controller is developed and used within the simulation solely to create the prescribed motion of the ITM-beam for control authority analysis and the determination of power requirements. Its purpose in this case is to match the ITM-beam oscillation frequency to the projectile roll rate within the simulation.

2.4 Description of Electromagnetic Actuator Control System. A zoom view of the ITM-beam mechanism is shown in Fig. 2. Two electromagnets, each at opposite ends of the cavity, exert force on the fixed magnet at the end of the ITM-beam.

The force exerted on a fixed magnetic dipole DM is given by [12,13]

$$f_{\text{input}} = DM\frac{\partial B_z}{\partial z_M} \tag{25}$$

The magnetic dipole moment per unit mass is a unique property of a material, with units joules/tesla/slug. For example, assuming the ITM is made of magnetized iron and using an ITM-beam mass of $m_T = 0.05$ slugs, the dipole moment is found to be $DM = 171.5$ J/T. The quantity $\partial B_z/\partial z_M$ can be found by first recognizing that the magnetic field B_z of an iron-core solenoid is given by the expression

$$B_z = \frac{I_E \mu k n}{2}\left[\frac{-z_M}{\sqrt{z_M^2 + b^2}} + \frac{z_M + L_A}{\sqrt{(z_M + L_A)^2 + b^2}}\right] \tag{26}$$

where I_E is the current through the electromagnet, μ is the magnetic constant ($4\pi \times 10^{-7}$ N/A^2), z_M is the distance from the end point of the ITM-beam to the nearest electromagnet actuator, k is the dimensionless relative permeability of iron (200 at a magnetic flux density of 0.002 W/m^2), n is the number of coils per meter, b is the radius of the solenoid, and L_A is the length of the solenoid. For all cases used below, values of 3 cm, 2 cm, and 10,000 were used respectively for b, L, and n. Taking the derivative of Eq. (26) with respect to z_M

Table 1 Relevant example projectile and ITM-beam properties

Projectile mass (slugs)	1.206
ITM-beam mass (slugs)	0.05
Projectile reference diameter (ft)	0.344
Projectile mass center position measured along the stationline (ft)	1.18
Projectile roll inertia (slugs ft^2)	0.0278
Projectile pitch inertia (slugs ft^2)	0.6291
ITM-beam length (BL) (ft)	0.3

$$\frac{\partial B_z}{\partial z_M} = \frac{I_E \mu k n}{2}\left[\frac{-1}{\sqrt{z_M^2 + b^2}} + \frac{z_M^2}{(z_M^2 + b^2)^{3/2}} + \frac{1}{\sqrt{(z_M + L_A)^2 + b^2}} - \frac{(z_M + L_A)^2}{((z_M + L_A)^2 + b^2)^{3/2}}\right] \tag{27}$$

At each timestep, the control force is computed using the feedback linearization. Knowing the magnetic dipole moment and the required control force, the quantity $\partial B_z/\partial z_M$ is computed at each timestep using Eq. (25). Then, knowing the position of the ITM-beam with respect to the actuators, the current required can be computed at each timestep by rearranging Eq. (27) such that

$$I_E = \frac{2}{k\mu n}\left[\frac{-1}{\sqrt{z_M^2 + b^2}} + \frac{z_M^2}{(z_M^2 + b^2)^{3/2}} + \frac{1}{\sqrt{(z_M + L_A)^2 + b^2}} - \frac{(z_M + L_A)^2}{((z_M + L_A)^2 + b^2)^{3/2}}\right]^{-1}\frac{\partial B_z}{\partial z_M} \tag{28}$$

Note that the electromagnet dimensions used above are comparable to dimensions for commercially-available iron-core electromagnets.

2.5 Description of Example Projectile. The example projectile used in all example simulations below is a representative fin-stabilized projectile. Relevant example projectile and ITM-beam dimensional and mass properties are outlined in Table 1. The hinge point is 0.9 ft behind the projectile mass center (P), and the ITM-beam oscillation amplitude is given by $BL\sin(\gamma_{\max}) = 0.157$ ft unless otherwise specified. In all the following cases the projectile is traveling through a standard atmosphere with no atmospheric wind.

3 Results

An example trajectory of the ITM-beam projectile is compared with an example trajectory of a projectile equipped with a strictly translating internal mass for model validation purposes. The translating mass projectile's dynamic equations are given in Ref. [10], and a previously validated model of this system was used for trajectory predictions. A diagram of the translating mass projectile is provided in Appendix B. Initial conditions used for the example trajectory were $x = 0.0$ ft, $y = 0.0$ ft, $z = 0.0$ ft, $u = 2821.0$ ft/s, $v = 0.0$ ft/s, $w = 0.0$ ft/s, $\phi = 1.5707$ rad, $\theta = 0.05$ rad, $\psi = 0.0$ rad, $p = 5.0$ rad/s, $q = 0.0$ rad/s, and $r = 0.0$ rad/s. The feedback linearization gains were $K_0 = 0.001$, $K_1 = 1000.0$, and $K_2 = 5 \times 10^5$. In all cases shown below, the ITM-beam oscillation frequency is locked to the projectile roll rate. Figures 3–6 show the trajectories for the ITM-beam projectile, the translating mass projectile, and the rigid projectile with no internal moving mass (denoted "Rigid 6DOF"). The two translating mass trajectories are generated solely to demonstrate control authority and to validate the ITM-beam simulation, and thus both controlled rounds are commanded to maximum possible deflection. Notice that the trajectories of the internal mass projectiles match nearly identically, even though the dynamic equations for the two systems are significantly different.

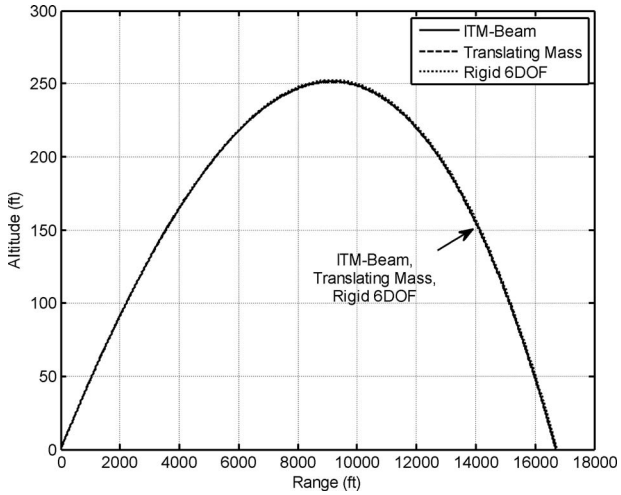

Fig. 3 Altitude versus range for example trajectory

The correlation between these two models serves as validation of the ITM-beam simulation.

Figure 7 shows a selected time history of ITM displacement from the projectile centerline. For the ITM-beam projectile, this displacement, denoted s_x, is given by

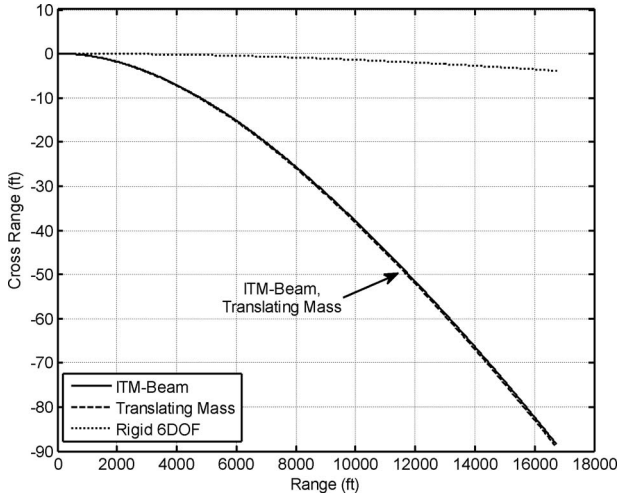

Fig. 4 Cross range versus range for example trajectory

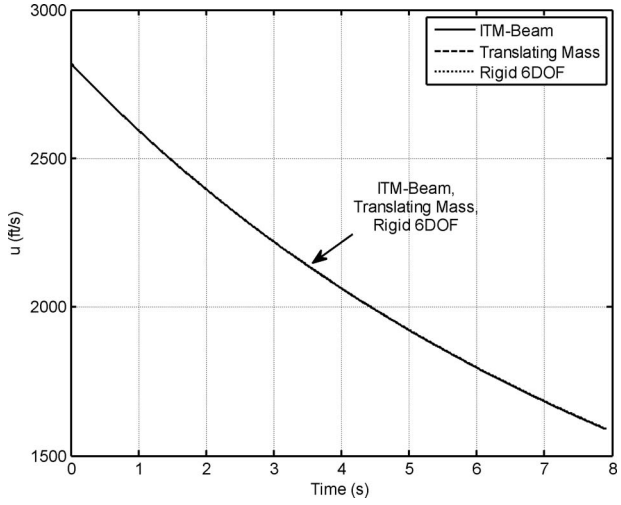

Fig. 5 *u* Velocity versus time for example trajectory

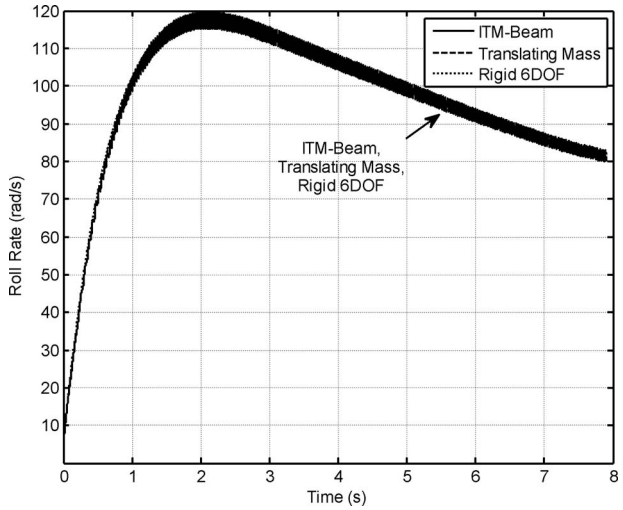

Fig. 6 Roll rate versus time for example trajectory. The thick lines represent high frequency oscillations, which occur only for the ITM-beam and translating mass case.

$$s_x = BL \sin(\gamma) \tag{29}$$

Notice that the two time histories for ITM displacement shown in Fig. 7 are nearly identical.

A control force time history for an example ITM-beam projectile simulation can be used, together with an ITM displacement time history, as shown in Fig. 7, to generate a time history of current required for each electromagnetic actuator. This is accomplished using the procedure outlined in Eqs. (25)–(28). Furthermore, this current time history can be integrated to produce the total charge required for a given example flight in A sec. This value for total charge can be used to size the battery for the ITM-beam control system. The total charge required for the example flight shown above was 13.5 A sec. Note that this number is relatively large since the spring and damper coefficient values have not been optimized for this preliminary example case.

Figure 8 shows a segment of the current time history for the example ITM-beam simulation used above. Notice that f_{input} (labeled "Force" in the plot) and the ITM displacement s_x are shown on the same plot as the current time history to demonstrate the phase relationships between current, input force, and ITM displacement. When the ITM-beam is displaced in the positive $\vec{I}_S$

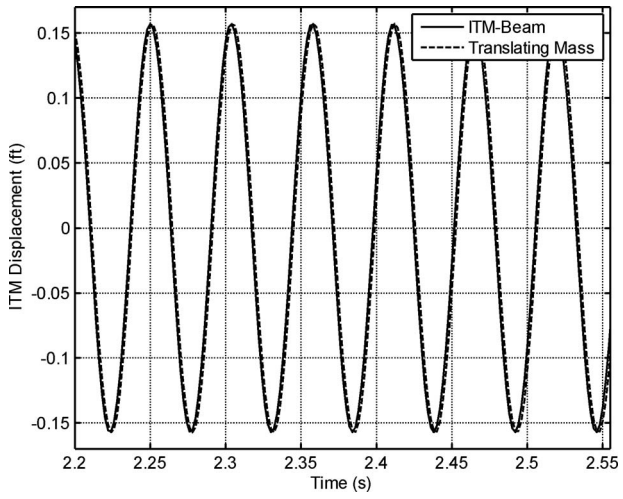

Fig. 7 Selected time history of ITM displacement from projectile centerline

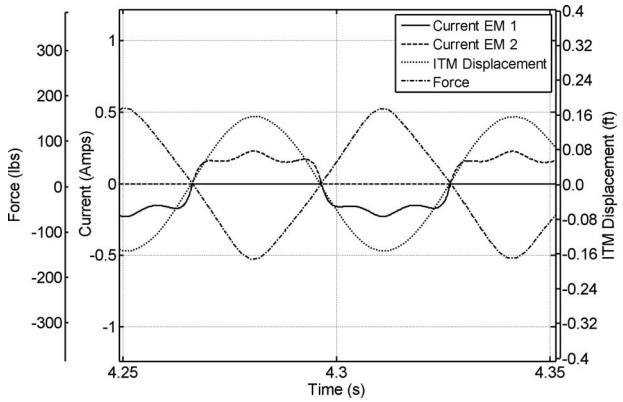

Fig. 8 Segment of current versus time for ITM-beam actuators

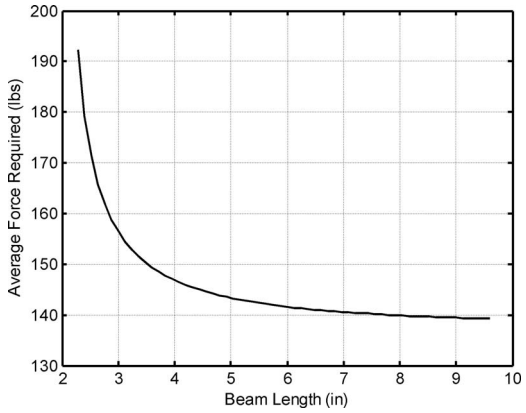

Fig. 10 Average force required versus beam length

direction (s_x positive), electromagnet EM 1 shuts off and EM 2 is responsible for control. Likewise, when the ITM-beam is displaced in the negative $\vec{I}_S$ direction (s_x negative), electromagnet EM 2 shuts off and EM 1 is responsible for control. This scheme takes advantage of the fact that the electromagnets are much more effective when the ITM is at close range. Since the current required is a nonlinear function of both distance to the ITM and control force required, the current time history is not sinusoidal like the ITM displacement and the control force time histories.

The length of the ITM-beam has a significant impact on the force required to move the beam in a prescribed fashion. From Eq. (18), the external moment exerted on the ITM-beam by the actuators in the $\vec{K}_S$ direction about point L is given by

$$\vec{K}_S \bullet \vec{M}^L_{\text{beam}} = -f_{\text{input}} BLc_\gamma \tag{30}$$

Therefore, the input force required to exert a given control moment on the ITM-beam varies inversely with beam length. In addition, for a given maximum ITM displacement s_x, the maximum angular displacement $\gamma_{\max}$ varies inversely with beam length. Trade studies verified these results using example simulations with various beam lengths. The maximum ITM displacement from the projectile centerline was $s_x = 0.157$ ft for all cases. Figures 9 and 10 show maximum angular displacement and average force required as a function of beam length, respectively. Notice that as beam length increases, maximum angular displacement and average force required both decrease. The average control force reduction with increased beam length occurs due to the increased "efficiency" of the ITM-beam actuators (i.e., the same control moment requires less control force for a larger beam length).

As outlined above, the ITM-beam system is a dynamic model used to represent a fixed-free elastic beam. The rigid ITM-beam is attached to the projectile at point L with a torsional spring and torsional damper to model the elastic beam's vibrational properties. A trade study examines how force and power requirements vary with different spring and damping coefficients. Once optimum spring and damper coefficient are determined, they can be used to identify the proper elastic properties of the fixed-free beam for a prototype system.

The performance of the system is examined for a range of torsional spring constants and damping ratios for the example projectile rolling at a steady-state rate of approximately 128 rad/s. The projectile trajectory is simulated for a 2 s flight with no gravity. This simplified flight profile is used solely to establish the correlation between spring and damper parameters and average force, average power, and total battery charge required. Figure 11 shows the projectile roll-rate time history for this flight profile. The high frequency oscillation of the roll rate occurs at the mass oscillation frequency. This is due to the continually-changing axial moment of inertia of the projectile as the mass translates. When the translating mass travels farther from the centerline, the axial inertia grows and the roll rate decreases due to conservation of angular momentum. Likewise, when the translating mass returns toward the centerline, the axial inertia decreases, and the roll rate increases.

Figures 12–14 show the effect of spring and damper coefficients on average force, average power, and total battery charge

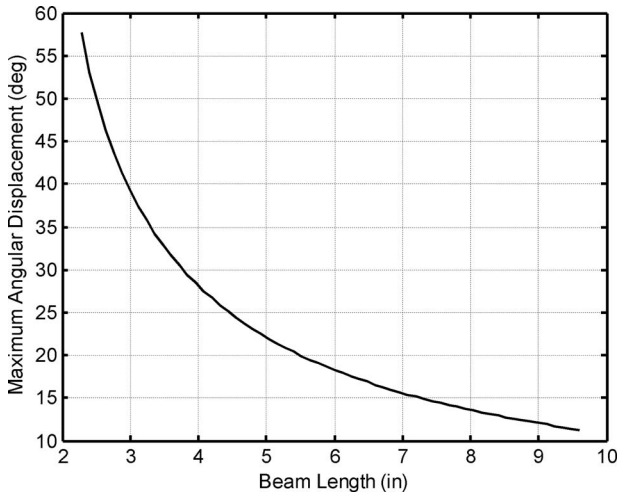

Fig. 9 Maximum displacement versus beam length

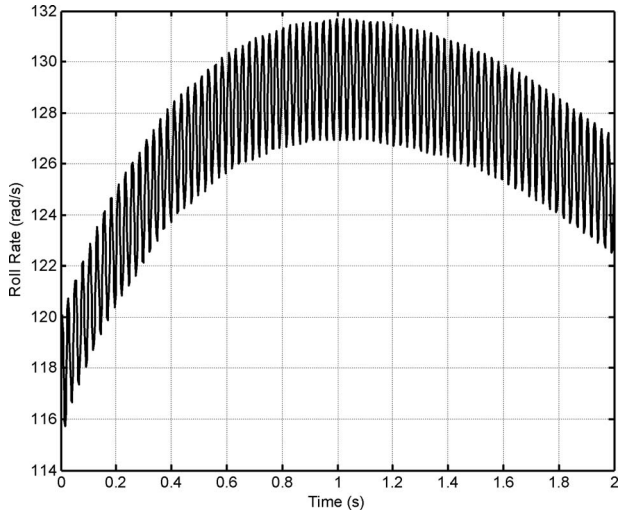

Fig. 11 Roll rate versus time for example simulation

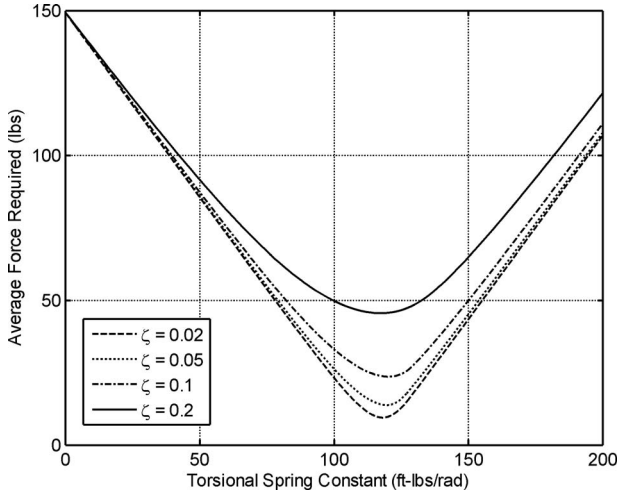

Fig. 12 Average force required versus torsional spring constant partial flight profile

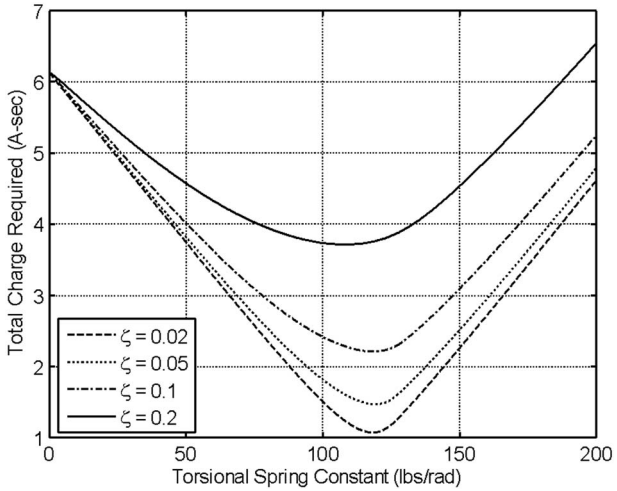

Fig. 14 Total charge required versus torsional spring constant partial flight profile

required. In Fig. 12, it can be clearly seen that an optimum torsional spring constant exists, in which the spring-mass-damper system of the ITM-beam operates near resonance with the projectile roll rate. These peaks are not as sharp as typical spring-mass-damper resonant peaks due to the fact that the projectile roll rate varies over time. Note, however, that significant reductions in force are achieved if the spring constant is placed near its optimum value and damping is lowered as much as possible. These reductions in force are mirrored by reductions in average power and total charge required, resulting in significantly smaller battery sizes.

A similar study examines the same spring-mass-damper parameters for a full flight profile of the example projectile using the same initial conditions as those used in the first example study above. Figures 15–17 show that, as in the partial flight profile case, optimal spring coefficients can be found.

However, the results for the partial flight profile have a significantly sharper peak than the results for the full flight profile. This is because, as shown in Fig. 6, the roll rate of the projectile varies between 5 rad/s initially and a final value of approximately 80 rad/s. This large variation in roll rate means that the spring coefficient is only optimized for a very short period of the overall flight, and the broad peaks shown in Figs. 15–17 result. To demonstrate this, Fig. 18 shows a current time history for an example full flight trajectory using k_T=70.0 lb/rad and k_D =0.05 lb/rad/s. Note that the spring constant is optimized for the projectile roll rate approximately 1 s into flight, and once again after spin decay occurs approximately 7 s into the flight.

Despite the broad nature of the peaks shown in Figs. 15–17, significant size and weight savings can be achieved using the proper spring constants in the form of smaller batteries. As shown in Fig. 17, batteries with a total charge of less than 5 A sec may be used for systems with optimal spring coefficients and low damping ratios. Furthermore, Fig. 18 shows that reasonable maximum current levels, on the order of 150 mA, can be expected with an optimized system.

Average force levels, and therefore total charge required, can be decreased even further by actively changing the elastic properties of the beam during flight. A fixed-free cantilever beam like that used in this system has a first vibrational mode shape of

$$s_x = \sin\left(\frac{\pi x_B}{2BL}\right) \tag{31}$$

where x_B is the distance along the beam. The natural frequency of the first vibrational mode is

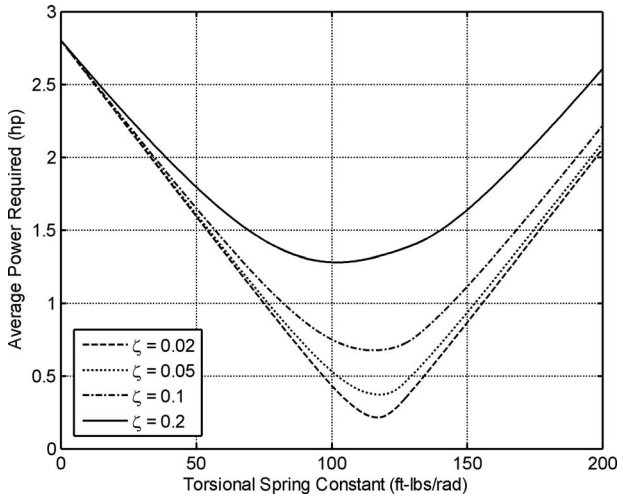

Fig. 13 Average power required versus torsional spring constant partial flight profile

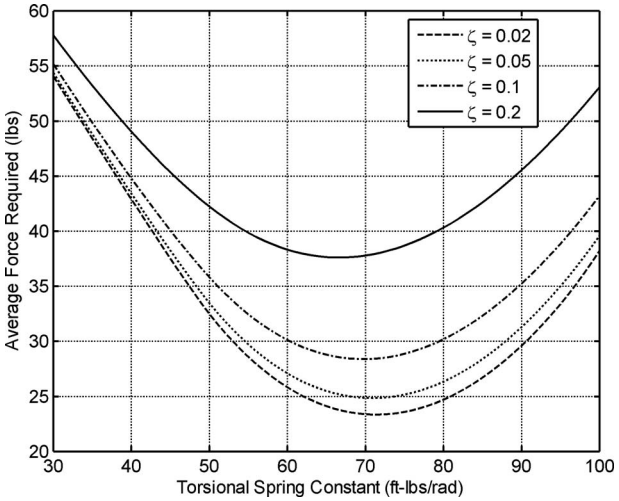

Fig. 15 Average force required versus torsional spring constant full flight profile

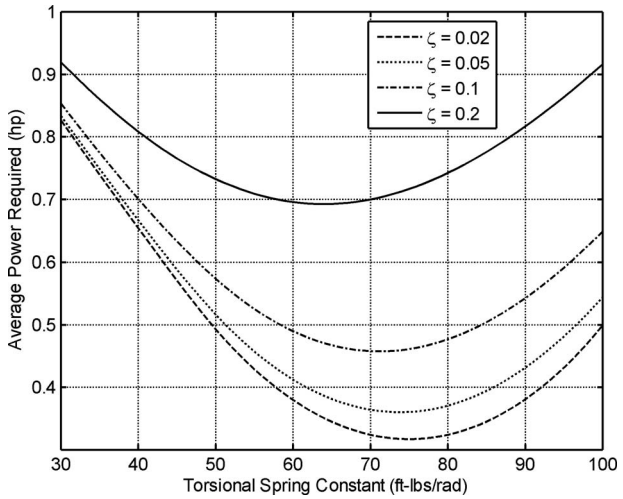

Fig. 16 Average power required versus torsional spring constant full flight profile

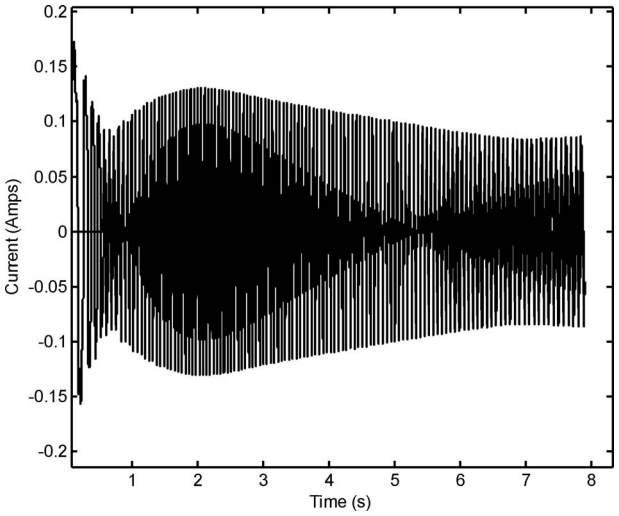

Fig. 18 Current through actuators versus time for example full flight trajectory

$$\omega_n = \frac{\pi}{2BL}\sqrt{\frac{E}{\rho}} \tag{32}$$

where E is the modulus of elasticity of the material and ρ is the density of the beam [14]. By changing the modulus of elasticity, it is therefore possible to tune the natural frequency of the cantilever beam to a desired value. Recent investigations into smart materials [15–18], specifically materials used in tunable vibration absorbers, have shown that various methods can be used to actively alter a material's modulus of elasticity, allowing the beam's torsional spring constant to be actively optimized during flight as the projectile roll rate changes. This would allow the ITM-beam system to operate with the lowest possible power through the entire flight, yielding further reductions in battery size.

To investigate this, several example simulations were run. The first set simulated the projectile for the full flight using the optimum spring constants obtained from Fig. 17. This produced the least possible battery charge required for the ITM-beam system with a fixed spring constant for each damping ratio considered. The second set of simulations included a roll-rate feedback mechanism. In these cases, at specific points throughout the flight the torsional spring and damping coefficients of the ITM-beam were adjusted to match the roll rate. Figure 19 shows how the torsional spring constant was adjusted for an example flight with ζ=0.05. Note that the curve in Fig. 19 has the same qualitative shape as the roll-rate time history shown in Fig. 6. Table 2 summarizes the results of the two sets of simulations with the fixed torsional spring and variable torsional spring constants. Note that in the variable torsional spring cases, the torsional damping coefficient k_D was adjusted slightly as well so as to keep the damping ratio ζ constant. Figure 20 demonstrates that implementation of the roll-rate feedback system saves approximately 1 A sec of

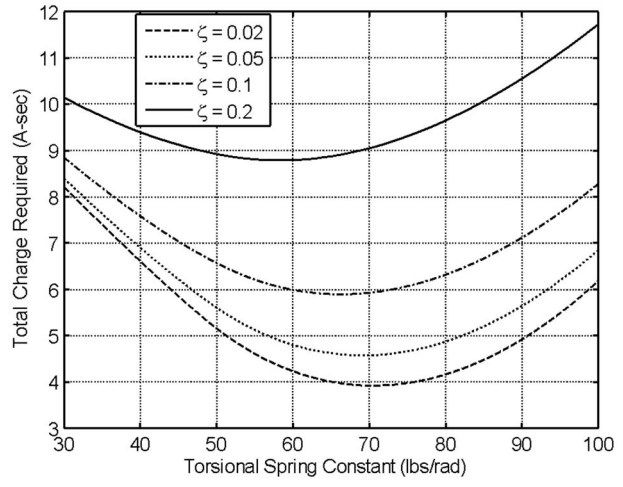

Fig. 17 Total charge required versus torsional spring constant full flight profile

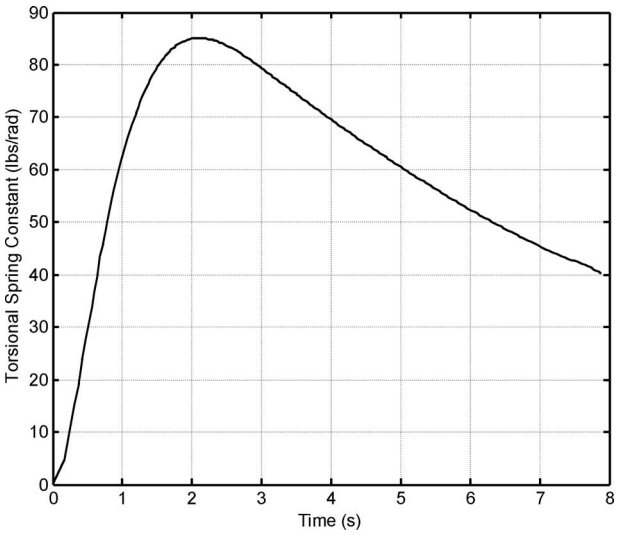

Fig. 19 Torsional spring constant versus time for roll-rate feedback system, ζ=0.05

Table 2 Performance evaluation of roll-rate feedback system

Damping ratio ζ	Optimum k_T for no feedback case	Charge required (mA h)		Percentage decrease in charge required with feedback (%)
		No feedback (constant k_T)	Feedback (variable k_T)	
0.02	71	3.924	2.576	34.4
0.05	69	4.576	3.287	28.1
0.1	67	5.895	4.692	20.4
0.2	58	8.786	7.798	11.2

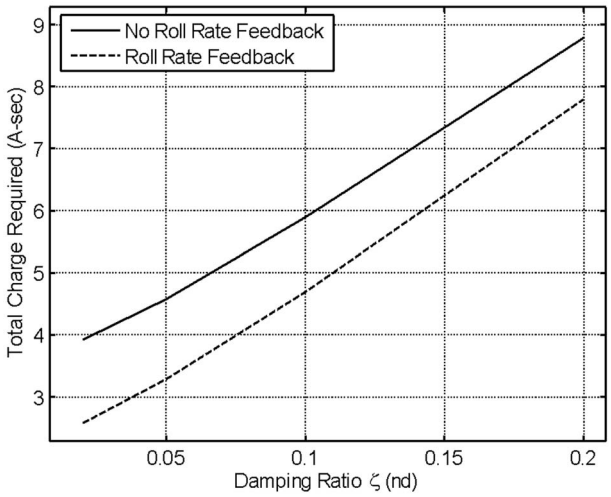

Fig. 20 Total charge required versus damping ratio for constant and variable k_T cases

charge for all damping ratios considered (34.4% decrease in battery size for ζ=0.02, 28.1% decrease for ζ=0.05, 20.4% for ζ=0.1, and 11.2% for ζ=0.2).

4 Conclusion

A conceptual design for a projectile equipped with a controllable internal mass is proposed using a cantilever beam configuration. The system is designed to minimize moving parts and to exploit the beam's elastic properties, thereby creating a robust mechanism that minimizes power requirements. A dynamic model of the configuration is developed, as is a model of the electromagnetic actuator system to study current requirements and battery size. Example simulations show that useful control authority is generated with this projectile control mechanism, matching the results from earlier studies of projectiles with internal translating mass control. Furthermore, by tuning the natural frequency of the vibrating beam to the projectile roll rate, significant reductions in power requirements are achieved on the order of 60%. Power reductions can be further realized with active tuning of the beam's elastic properties during flight. Battery size requirements to power the actuator are modest, with several COTS options available. The internal oscillating beam configuration shows promise as a viable, cost effective, reliable projectile control mechanism.

Nomenclature

a_1, a_2, and a_3 = components in the S frame of the acceleration of the system mass center with respect to the inertial frame

$\vec{a}_{P/I}$ = acceleration of the projectile mass center with respect to the inertial frame

$\vec{a}_{X/I}$ = acceleration of the end of the ITM-beam with respect to the inertial frame

A = maximum magnitude of ITM-beam displacement from center of cavity

b = radius of the electromagnetic actuator

BL = length of the ITM-beam assembly

$\vec{B}_z$ = magnetic field produced by the electromagnetic actuators in the $\vec{I}_S$ direction

C = composite body center of mass

DM = magnitude of the magnetic dipole moment of the fixed magnet at the end of the ITM-beam

$\vec{F}_C$ = hinge constraint force on the internal translating mass

$\vec{F}_I$ = input force exerted by electromagnetic actuators on ITM-beam

$\vec{F}_P$ = total aerodynamic force exerted on the projectile

f_{input} = scalar value of the total force applied to ITM-beam by electromagnetic actuators

$\vec{H}^P_{B/I}$ = angular momentum of the projectile with respect to the inertial frame about the projectile center of mass

$\vec{H}^X_{T/I}$ = angular momentum of the ITM-beam with respect to the inertial frame about point X

I_{Txx} = the xx component of the ITM-beam moment of inertia matrix about point X

I_{Pxx} = the xx component of the projectile moment of inertia matrix

$\vec{I}_I$, $\vec{J}_I$, and $\vec{K}_I$ = inertial frame unit vectors

$\vec{I}_B$, $\vec{J}_B$, and $\vec{K}_B$ = projectile reference frame unit vectors

$\vec{I}_N$, $\vec{J}_N$, and $\vec{K}_N$ = nonrolling reference frame unit vectors

$\vec{I}_T$, $\vec{J}_T$, and $\vec{K}_T$ = ITM-beam fixed frame unit vectors

$\vec{I}_S$, $\vec{J}_S$, and $\vec{K}_S$ = S frame unit vectors

I_E = current through the electromagnetic actuator

k_D = torsional damper coefficient

k_T = torsional spring coefficient

L = junction of between the ITM-beam and the projectile, referred to as the "hinge point"

L_A = length of the electromagnetic actuator

m_P = mass of the projectile with the cavity

m_T = mass of the ITM-beam

m = total mass of the system

$\vec{M}^L_P$ = external moments applied to the projectile about the hinge point L

$\vec{M}^L_{\text{system}}$ = external moments applied to the projectile-ITM system about the hinge point L

$\vec{M}^L_{\text{beam}}$ = external moment exerted on the ITM-beam by the actuators in the $\vec{K}_S$ direction about the hinge point L

P = projectile center of mass

$\vec{r}_{L\to X}$ = distance vector from the hinge point L to point X at the end of the ITM-beam

$\vec{r}_{L\to P}$ = distance vector from the hinge point L to the projectile center of mass P

$\vec{r}_{P\to X}$ = distance vector from projectile center of mass P to point X at the end of the ITM-beam

r_1, r_2, and r_3 = components in the S frame of $\vec{r}_{P\to L}$

r_4, r_5, and r_6 = components in the S frame of $\vec{r}_{P\to X}$

$\tilde{p}$, $\tilde{q}$, and $\tilde{r}$ = components of $\vec{\omega}_{B/I}$ in the S frame

p, q, and r = components of $\vec{\omega}_{B/I}$ in the projectile reference frame

u, v, and w = translational velocity components of the composite body center of mass resolved in the projectile reference frame

$\vec{v}_{C/I}$ = velocity of the system mass center with respect to the inertial frame

$\vec{W}_P$ = weight of the projectile (without the ITM-beam)

$\vec{W}_T$ = weight of the ITM-beam

X = point at the end of the ITM-beam

x, y, and z = position vector components of the composite body center of mass expressed in the inertial reference frame

X_B, Y_B, and Z_B = total external force components on the projectile and ITM-beam system expressed in the projectile reference frame

$\vec{\alpha}_{B/I}$ = angular acceleration of the projectile body with respect to the inertial frame

$\vec{\alpha}_{T/I}$ = angular acceleration of the ITM-beam with respect to the inertial frame

γ = deflection angle of the ITM-beam

ϕ, θ, and ψ = Euler roll, pitch, and yaw angles

θ_T and ψ_T = Euler pitch and yaw angles for the orientation of the S frame with respect to the B frame

$\vec{\omega}_{B/I}$ = angular velocity of the projectile body with respect to the inertial frame

$\vec{\omega}_{T/I}$ = angular velocity of the ITM-beam with respect to the inertial frame

ω_{beam} = magnitude of the angular velocity of the ITM-beam with respect to the S frame

Appendix A

The terms of Eq. (22) are given as follows:

$$A_{11} = I_{T31} + BL\frac{m_P m_T}{m} s_\gamma r_3$$

$$A_{12} = I_{T32} - BL\frac{m_P m_T}{m} c_\gamma r_3$$

$$A_{13} = I_{T33} + BL^2\frac{m_P m_T}{m} + BL\frac{m_P m_T}{m}(c_\gamma r_2 - s_\gamma r_1)$$

$$A_{14} = I_{T33} + BL^2\frac{m_P m_T}{m}$$

$$A_{21} = I_{P31} - \frac{m_P m_T}{m} r_1 r_3$$

$$A_{22} = I_{P32} - \frac{m_P m_T}{m} r_2 r_3$$

$$A_{23} = I_{P33} + \frac{m_P m_T}{m} BL(r_2 c_\gamma - r_1 s_\gamma) + \frac{m_P m_T}{m}(r_1^2 + r_2^2)$$

$$A_{24} = \frac{m_P m_T}{m} BL(r_2 c_\gamma - r_1 s_\gamma)$$

$$A_{31} = I_{P21} + I_{T21} - \frac{m_P m_T}{m} BLr_4 c_\gamma - \frac{m_P m_T}{m} r_2 r_4$$

$$A_{32} = I_{P22} + I_{T22} - \frac{m_P m_T}{m} BLr_4 s_\gamma + \frac{m_P m_T}{m}(r_1 r_4 + r_3 r_6)$$

$$A_{33} = I_{P23} + I_{T23} - \frac{m_P m_T}{m} BLr_6 c_\gamma - \frac{m_P m_T}{m} r_2 r_6$$

$$A_{34} = I_{T23} - \frac{m_P m_T}{m} BLr_6 c_\gamma$$

$$A_{41} = I_{P11} + I_{T11} + \frac{m_P m_T}{m} BLr_5 c_\gamma + \frac{m_P m_T}{m}(r_2 r_5 + r_3 r_6)$$

$$A_{42} = I_{P12} + I_{T12} + \frac{m_P m_T}{m} BLr_5 s_\gamma - \frac{m_P m_T}{m} r_1 r_5$$

$$A_{43} = I_{P13} + I_{T13} + \frac{m_P m_T}{m} BLr_6 s_\gamma - \frac{m_P m_T}{m} r_1 r_6$$

$$A_{44} = I_{T13} + \frac{m_P m_T}{m} BLr_6 s_\gamma$$

$$\begin{aligned} B_1 = &- \vec{K}_S \bullet \mathrm{S}(\vec{r}_{L\to X}) m_T \mathrm{C}_S(\vec{a}_{C/I}) - f_{\text{input}} BLc_\gamma - k_T\gamma - k_D\dot{\gamma} \\ &- \vec{K}_S \bullet \mathrm{S}(\vec{\omega}_{B/I}) I_T \mathrm{C}_S(\vec{\omega}_{T/I}) + \vec{K}_S \bullet \mathrm{S}(\vec{r}_{L\to X}) \mathrm{C}_S(\vec{W}_T) \\ &- \frac{m_P m_T}{m} \vec{K}_S \bullet \mathrm{S}(\vec{r}_{L\to X}) \mathrm{S}(\vec{\omega}_{T/I}) \mathrm{S}(\vec{\omega}_{T/I}) \mathrm{C}_T(\vec{r}_{L\to X}) \\ &- \frac{m_P m_T}{m} \vec{K}_S \bullet \mathrm{S}(\vec{r}_{L\to X}) \mathrm{S}(\vec{\omega}_{B/I}) \mathrm{S}(\vec{\omega}_{B/I}) \mathrm{C}_S(\vec{r}_{P\to L}) \\ &- \frac{m_P m_T}{m} \vec{K}_S \bullet \mathrm{S}(\vec{r}_{L\to X}) [\mathrm{S}(\vec{\omega}_{B/I}) \times \mathrm{C}_S(\vec{\omega}_{T/I})] \times \mathrm{C}_S(\vec{r}_{L\to X}) \end{aligned}$$

$$\begin{aligned} B_2 = &- \vec{K}_S \bullet m_P \mathrm{S}(\vec{r}_{L\to P}) \mathrm{C}_S(\vec{a}_{C/I}) + f_{\text{input}} BLc_\gamma + k_T\gamma + k_D\dot{\gamma} \\ &- \vec{K}_S \bullet \mathrm{S}(\vec{\omega}_{B/I}) I_P \mathrm{C}_S(\vec{\omega}_{B/I}) + \vec{K}_S \bullet \mathrm{C}_S\left(\sum \vec{M}_P^L\right) \\ &+ \frac{m_P m_T}{m} \vec{K}_S \bullet \mathrm{S}(\vec{r}_{L\to P}) \mathrm{S}(\vec{\omega}_{T/I}) \mathrm{S}(\vec{\omega}_{T/I}) \mathrm{C}_S(\vec{r}_{L\to X}) \\ &+ \frac{m_P m_T}{m} \vec{K}_S \bullet \mathrm{S}(\vec{r}_{L\to P}) \mathrm{S}(\vec{\omega}_{B/I}) \mathrm{S}(\vec{\omega}_{B/I}) \mathrm{C}_S(\vec{r}_{P\to L}) \\ &+ \frac{m_P m_T}{m} \vec{K}_S \bullet \mathrm{S}(\vec{r}_{L\to P}) [\mathrm{S}(\vec{\omega}_{B/I}) \times \mathrm{C}_S(\vec{\omega}_{T/I})] \times \mathrm{C}_S(\vec{r}_{L\to X}) \\ &+ \vec{K}_S \bullet \mathrm{S}(\vec{r}_{L\to P}) \mathrm{C}_S(\vec{W}_P) \end{aligned}$$

$$\begin{aligned} B_3 = &- \vec{J}_S \bullet \mathrm{S}(\vec{\omega}_{B/I}) I_P \mathrm{C}_S(\vec{\omega}_{B/I}) - \vec{J}_S \bullet \mathrm{C}(\vec{\omega}_{T/I}) I_T \mathrm{C}_S(\vec{\omega}_{T/I}) \\ &+ \vec{J}_S \bullet \mathrm{S}(\vec{r}_{L\to X}) \mathrm{C}_S(\vec{W}_T) - \vec{J}_S \bullet m\mathrm{S}(\vec{r}_{L\to P}) \mathrm{C}_S(\vec{a}_{C/I}) \\ &- \vec{J}_S \bullet m_T \mathrm{S}(\vec{r}_{P\to X}) \mathrm{C}_S(\vec{a}_{C/I}) \\ &- \frac{m_P m_T}{m} \vec{J}_S \bullet \mathrm{S}(\vec{r}_{P\to X}) \mathrm{S}(\vec{\omega}_{T/I}) \mathrm{S}(\vec{\omega}_{T/I}) \mathrm{C}_S(\vec{r}_{L\to X}) \\ &- \frac{m_P m_T}{m} \vec{J}_S \bullet \mathrm{S}(\vec{r}_{P\to X}) \mathrm{S}(\vec{\omega}_{B/I}) \mathrm{S}(\vec{\omega}_{B/I}) \mathrm{C}_S(\vec{r}_{P\to L}) \\ &+ \vec{J}_S \bullet \mathrm{C}_S\left(\sum \vec{M}_{\text{system}}^L\right) - \frac{m_P m_T}{m} \vec{J}_S \bullet \mathrm{S}(\vec{r}_{P\to X}) [\mathrm{S}(\vec{\omega}_{B/I}) \mathrm{C}_S(\vec{\omega}_{T/I})] \\ &\times \mathrm{C}_S(\vec{r}_{L\to X}) \end{aligned}$$

$$\begin{aligned} B_4 = &- \vec{I}_S \bullet \mathrm{S}(\vec{\omega}_{B/I}) I_P \mathrm{C}_S(\vec{\omega}_{B/I}) - \vec{I}_S \bullet \mathrm{S}(\vec{\omega}_{T/I}) I_T \mathrm{C}_S(\vec{\omega}_{T/I}) \\ &+ \vec{I}_S \bullet \mathrm{S}(\vec{r}_{L\to X}) \mathrm{C}_S(\vec{W}_T) - \vec{I}_S \bullet m\mathrm{S}(\vec{r}_{L\to P}) \mathrm{C}_S(\vec{a}_{C/I}) \\ &- \vec{I}_S \bullet m_T \mathrm{S}(\vec{r}_{P\to X}) \mathrm{C}_S(\vec{a}_{C/I}) \\ &- \frac{m_P m_T}{m} \vec{I}_S \bullet \mathrm{S}(\vec{r}_{P\to X}) \mathrm{S}(\vec{\omega}_{T/I}) \mathrm{S}(\vec{\omega}_{T/I}) \mathrm{C}_S(\vec{r}_{L\to X}) \\ &- \frac{m_P m_T}{m} \vec{I}_S \bullet \mathrm{S}(\vec{r}_{P\to X}) \mathrm{S}(\vec{\omega}_{B/I}) \mathrm{S}(\vec{\omega}_{B/I}) \mathrm{C}_S(\vec{r}_{P\to L}) \\ &+ \vec{I}_S \bullet \mathrm{C}_S\left(\sum \vec{M}_{\text{system}}^L\right) - \frac{m_P m_T}{m} \vec{I}_S \bullet \mathrm{S}(\vec{r}_{P\to X}) [\mathrm{S}(\vec{\omega}_{B/I}) \mathrm{C}_S(\vec{\omega}_{T/I})] \\ &\times \mathrm{C}_S(\vec{r}_{L\to X}) \end{aligned}$$

$$\begin{aligned} B_{FLC} = &- \vec{K}_S \bullet \mathrm{S}(\vec{r}_{L\to X}) m_T \mathrm{C}_S(\vec{a}_{C/I}) - k_T\gamma - k_D\dot{\gamma} \\ &- \vec{K}_S \bullet \mathrm{S}(\vec{\omega}_{B/I}) I_T \mathrm{C}_S(\vec{\omega}_{T/I}) + \vec{K}_S \bullet \mathrm{S}(\vec{r}_{L\to X}) \mathrm{C}_S(\vec{W}_T) \\ &- \frac{m_P m_T}{m} \vec{K}_S \bullet \mathrm{S}(\vec{r}_{L\to X}) \mathrm{S}(\vec{\omega}_{T/I}) \mathrm{S}(\vec{\omega}_{T/I}) \mathrm{C}_T(\vec{r}_{L\to X}) \end{aligned}$$

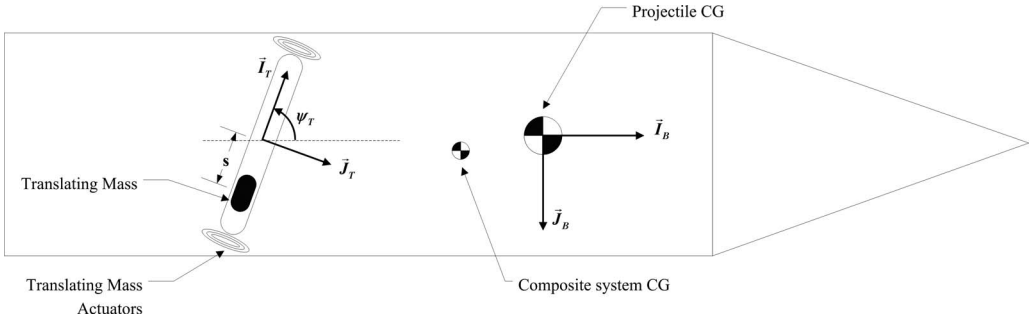

Fig. 21 Translating mass projectile schematic

$$-\frac{m_P m_T}{m}\vec{K}_S \bullet \mathbb{S}(\vec{r}_{L\to X})\mathbb{S}(\vec{\omega}_{B/I})\mathbb{S}(\vec{\omega}_{B/I})\mathbb{C}_S(\vec{r}_{P\to L})$$

$$-\frac{m_P m_T}{m}\vec{K}_S \bullet \mathbb{S}(\vec{r}_{L\to X})[\mathbb{S}(\vec{\omega}_{B/I}) \times \mathbb{C}_S(\vec{\omega}_{T/I})] \times \mathbb{C}_S(\vec{r}_{L\to X})$$

Appendix B

Figure 21 is a schematic of the translating mass projectile.

References

[1] Soper, W., 1978, "Projectile Instability Produced by Internal Friction," AIAA J., **16**(1), pp. 8–11.

[2] Murphy, C., 1978, "Influence of Moving Internal Parts on Angular Motion of Spinning Projectiles," J. Guid. Control, **1**(2), pp. 117–122.

[3] D'Amico, W., 1987, "Comparison of Theory and Experiment for Moments Induced by Loose Internal Parts," J. Guid. Control, **10**(1), pp. 14–19.

[4] Hodapp, A., 1989, "Passive Means for Stabilizing Projectiles With Partially Restrained Internal Members," J. Guid. Control, **12**(2), pp. 135–139.

[5] Petsopoulos, T., Regan, F., and Barlow, J., 1996, "Moving Mass Roll Control System for Fixed-Trim Re-Entry Vehicle," J. Spacecr. Rockets, **33**(1), pp. 54–61.

[6] Robinett, R., Sturgis, B., and Kerr, S., 1996, "Moving Mass Trim Control for Aerospace Vehicles," J. Guid. Control Dyn., **19**(5), pp. 1064–1071.

[7] Menon, P., Sweriduk, G., Ohlmeyer, E., and Malyevac, D., 2004, "Integrated Guidance and Control of Moving Mass Actuated Kinetic Warheads," J. Guid. Control Dyn., **27**(1), pp. 118–127.

[8] Frost, G., and Costello, M., 2004, "Linear Theory of a Projectile With a Rotating Internal Part in Atmospheric Flight," J. Guid. Control Dyn., **27**(5), pp. 898–906.

[9] Frost, G., and Costello, M., 2006, "Control Authority of a Projectile Equipped With an Internal Unbalanced Part," ASME J. Dyn. Syst., Meas., Control, **128**(4), pp. 1005–1012.

[10] Rogers, J., and Costello, M., 2008, "Control Authority of a Projectile Equipped With an Internal Translating Mass," J. Guid. Control Dyn., **31**(5), pp. 1323–1333.

[11] Slotine, J., and Li, W., 1991, *Applied Nonlinear Control*, Prentice-Hall, Englewood Cliffs, NJ, pp. 207–236.

[12] Purcell, E., 1985, *Electricity and Magnetism*, McGraw-Hill, New York, pp. 227.

[13] Purcell, E., 1985, *Electricity and Magnetism*, McGraw-Hill, New York, pp. 412–138.

[14] Inman, D., 2001, *Engineering Vibration*, Prentice Hall, p. 451.

[15] Flatau, A., Dapino, M., and Calkins, F., 2000, "High Bandwidth Tunability in a Smart Vibration Absorber," J. Intell. Mater. Syst. Struct., **11**, pp. 923–929.

[16] Varga, Z., Filipcsei, G., and Zrinyi, M., 2005, "Smart Composites With Controlled Anisotropy," Polymer, **46**, pp. 7779–7787.

[17] Varga, Z., Filipcsei, G., and Zrinyi, M., 2006, "Magnetic Field Sensitive Functional Elastomers With Tuneable Elastic Modulus," Polymer, **47**, pp. 227–233.

[18] Davis, C., and Lesieutre, G., 2000, "An Actively Tuned Solid-State Vibration Absorber Using Capacitive Shunting of Piezoelectric Stiffness," J. Sound Vib., **232**(3), pp. 601–617.